Integrated Simulations of Implosion, Electron Transport, and Heating for Direct-Drive Fast-Ignition Targets

Introduction

In fast-ignition[1] inertial confinement fusion (ICF), a cryogenic shell of deuterium and tritium (DT) is first imploded by a high-energy driver to produce an assembly of thermonuclear fuel with high densities and areal densities. Such a dense core is then ignited by the fast electrons (or protons) accelerated through the interaction of a high-power, ultra-intense laser pulse with either a coronal plasma or a solid cone-shaped target.[2,3] The separation of the target compression and ignition stages in fast ignition relaxes the requirements on the symmetry of the implosion and compression energy. By using massive cryogenic targets,[4] fast ignition has the potential for gains higher than the conventional ICF central hot-spot ignition scheme.

Fast ignition has shown significant promise in successful small-scale integrated experiments[2] that combine implosions of plastic cone-in-shell targets and heating by subpetawatt laser pulses. The next generation of integrated fast-ignition experiments will use more-massive plastic or cryogenic-DT cone-in-shell targets heated by more-powerful petawatt laser pulses. Such experiments have started at LLE and are planned at other facilities, such as ILE (Osaka University), NIF (LLNL), and the HiPER project. The success of those experiments depends crucially on the understanding of fast-ignition physics and its careful modeling using the best-available numerical codes. The rich physics of fast ignition includes processes having very different temporal and spatial scales, which must be studied using different types of codes. Target implosions are simulated using hydrocodes. Generation of hot electrons by a petawatt laser pulse is simulated using particle-in-cell (PIC) codes. Transport of hot electrons to the dense core is simulated using hybrid-PIC, Monte Carlo, or Fokker−Plank codes. Ignition and burn require simulations of fusion reactions, α-particle transport, and target hydrodynamics, which are done using hydrocodes.

At LLE a comprehensive theory and simulation program is being pursued to explore the physics of fast ignition. High-gain fast-ignition targets have been developed based on hydrodynamic simulations of implosion,[4] and performance of those targets has been investigated using hydrodynamic and hybrid simulations.[5,6] The capabilities of the radiation-hydrodynamic code *DRACO*,[7] developed at LLE to study the implosion physics, have been recently extended to simulate cone-in-shell targets.[8] *DRACO* has also been recently integrated with the hybrid-PIC code *LSP*[9] to simulate the hot-electron transport, target heating, and ignition.[6]

This article reports the latest results from integrated simulations of implosion, hot-electron transport, and heating, for direct-drive, cone-in-shell surrogate plastic targets used in the integrated fast-ignition experiments at LLE, performed using *DRACO* and *LSP*. *LSP* simulations of planar plastic targets are also presented. An important effect found in the simulations is the collimation of hot electrons by the self-generated resistive magnetic field. This effect appears to be highly beneficial for fast ignition because hot electrons are generated in the petawatt laser interaction with a solid-density plasma of the cone tip with an inevitable angular spread.[10,11] In the absence of collimation there is little hope to deliver the energy by hot electrons into a small volume of the target core with a radius of about 20 μm, located tens or even hundreds of μm away from the cone tip.[5,12,13] Magnetic collimation of hot electrons increases their coupling with the core and thus decreases the minimum energy required for ignition.

The following sections describe (1) *DRACO* and *LSP*, the two codes used in the simulations; (2) *LSP* simulations of hot-electron transport in solid-density and compressed plastic targets, providing a connection between the recent solid-target experiments and near-future integrated fast-ignition experiments using imploded plastic shells; and (3) the results from integrated simulations of realistic cone-in-shell plastic (CD) targets used in the integrated fast-ignition experiments at LLE, predicting target heating by hot electrons and neutron yields from deuterium−deuterium (D−D) nuclear reactions. The last section summarizes conclusions.

DRACO, LSP, and Integrated DRACO–LSP Simulation Toolkit

DRACO[7] is a two-dimensional (2-D) axisymmetric radiation-hydrodynamic code developed at LLE. It includes the physics required to simulate implosion, ignition, and burn of direct-drive ICF targets. It includes radiation transport and uses realistic equations of state. *LSP*[9] (large-scale plasma) is a 2-D/3-D (three-dimensional) implicit hybrid-PIC code. It uses an implicit solution for the electromagnetic fields and an implicit particle push, hybrid fluid-kinetic description for plasma electrons with dynamic reallocation, intra- and interspecies collisions based on Spitzer rates, and an ideal-gas equation of state. The hybrid fluid-kinetic description for plasma electrons is especially suited for modeling the hot-electron transport in the fast-ignition scheme. Fluid species can be used for background plasma electrons (and ions) while kinetic species are required to describe energetic electrons. The temperature equation solved for fluid species provides good energy conservation in the modeling of plasma heating by hot electrons. An implicit algorithm in *LSP* provides numerical stability even for very dense plasmas, when the numerical time step greatly exceeds the period of plasma oscillations (high-frequency phenomena, however, are not resolved).

The collisional model in *LSP* was modified to include relativistic and high-density plasma effects and extensively tested to reproduce the correct ranges, blooming, and straggling of hot electrons, as predicted by Refs. 14 and 15. The collisional model uses new recalculated transport scattering coefficients for hot electrons, obtained using the relativistic Rutherford-scattering cross section.[16] The transport coefficients for hot electrons are also modified to account for the electron energy loss caused by incoherent excitation of plasma waves.[14] The fluid electron–ion Spitzer collisional rate is modified to saturate at low electron temperatures to reproduce the appropriate maximum electrical resistivities.[17] For compressed materials, the fluid electron-ion Spitzer collisional rate is saturated below the Fermi-degenerate temperature $\left[\hbar^2\left(\pi^2 n_e\right)^{2/3}\middle/3^{1/3}m_e\right]$, which can be hundreds of eV for compressed DT or plastic fast-ignition targets. The Coulomb logarithms in the Spitzer rates are modified to include ion strong-coupling and electron-degeneracy corrections as suggested in Ref. 18. Since, in the collisional model in *LSP*, each species is approximated by a single drifting (relativistic) Maxwellian distribution, simulations in this article use separate species for hot electrons in different energy ranges. This ensures that correct scattering and slowing-down rates are used for hot electrons at different energy levels.

The *DRACO* and *LSP* codes have been recently integrated and used to simulate electron transport and ignition for spherically symmetric cryogenic-DT, high-gain, fast-ignition targets.[6] In the integrated simulations, *LSP* generates the hot-electron source term in the temperature equation for background plasma electrons, solved in *DRACO*. In the simulations of Ref. 6, a self-generated resistive magnetic field was found to collimate the hot electrons and reduce the minimum energy required for ignition, in agreement with Ref. 19. The minimum hot-electron-beam energy of 43 kJ was found to be necessary for ignition using Gaussian electron beams with a mean electron energy of 2 MeV and a divergence half-angle of 20°. Collimation is less effective for electron beams with a larger divergence half-angle.

Simulations of Hot-Electron Transport in Solid-Density and Compressed Plastic Targets

In cone-guided fast ignition, hot electrons are generated by the petawatt laser pulse interacting with the tip of a gold cone about a hundred or more microns away from the dense target core. The transport of hot electrons to the dense core is possible if the beam current of about 1 GA, greatly exceeding the Alfvén limit, is compensated by the return current of plasma electrons. Most present experiments that study the transport of hot electrons in such conditions use solid-density metallic, plastic, or glass targets. The transport properties of hot electrons in those materials can be significantly different than in the compressed hydrogenic plasmas of fast-ignition targets, for instance, due to very different values of the electrical resistivities.

For a 300-g/cm^3 plasma, the hot-electron beam energy required for ignition is minimized when the beam radius on target is about 20 μm (Refs. 5, 12, and 13), approximately the minimum size of the laser spot on target. Since hot electrons are generated with an intrinsic angular spread, some collimation mechanism is necessary for the electron-beam radius to remain constant when it reaches the dense core. Collimation of hot electrons was observed in the plastic- and glass-target experiments using relatively low energy laser pulses of a few tens of joules.[20–22] More recent experiments (see Ref. 10 and references therein) using more-energetic laser pulses up to a few hundred joules and metallic (usually aluminum or copper) or plastic targets did not show collimation, with the divergence angle of hot electrons found to increase with the laser pulse intensity (see, for instance, Fig. 2 of Ref. 10). Hot-electron collimation in the experiments of Refs. 20–22 was explained by the presence of self-generated resistive magnetic fields.[23,24]

We have performed *LSP* simulations of hot-electron transport in solid-density plastic plasmas ($\rho \approx 1$ g/cm^3) containing hydrogen ions H^+ and four-times-ionized carbon ions C^{4+}. The Spitzer plasma resistivity[25] was saturated at low temperatures according to $\eta = 1/\sqrt{\eta_{max}^{-2} + \eta_{Sp}^{-2}}$, where[17] $\eta_{max} = 3 \times 10^{-6}$ Ωm. Figures 117.28–117.30 show the results of 2-D planar geometry simulations performed for three different laser-pulse intensities. The laser pulses are Gaussian in space and in time with a focal-spot diameter of 10 μm, full width at half maximum (FWHM), and duration of 1 ps. The maximum intensities in the simulations of Figs. 117.28–117.30 are 5×10^{18} W/cm^2, 2×10^{19} W/cm^2, and 6×10^{19} W/cm^2, respectively. The laser wavelength is $\lambda_0 = 1.054$ μm. Hot electrons are promoted from the background of plasma electrons at the left-hand-side plasma boundary, having an exponential energy distribution $\left[\exp(-E/\langle E \rangle)\right]$. The mean energy is given by the maximum of the ponderomotive[26] and Beg's[27] scaling

$$\langle E \rangle [\text{MeV}] = \max\left\{ 0.511\left[\left(1 + I\lambda_0^2/2.8 \times 10^{18}\right)^{1/2} - 1\right],\right.$$

$$\left. 0.1\left(I\lambda_0^2/10^{17}\right)^{1/3}\right\},$$

where I is the local instantaneous value of the laser intensity in W/cm^2 and λ_0 is in μm. The energy-conversion efficiency to hot electrons is given by[28]

$$\eta_h = 1.75 \times 10^{-6} I^{0.2661}.$$

Hot electrons are injected in the plane of simulation at a random angle toward the beam axis, having a Gaussian distribution and a mean half-angle of 30°, half width at half maximum (HWHM). (Such a divergence half-angle is consistent with recent particle-in-cell simulations of hot-electron generation by a petawatt laser pulse.[10,11])

Snapshots of the hot-electron-beam density and magnetic field 700 fs after the peak of the laser pulse are shown in Figs. 117.28–117.30. It is seen that the hot-electron beam is sufficiently well collimated by the self-generated resistive magnetic field in the simulation of Fig. 117.28, while it is only partially collimated in the simulations of Figs. 117.29 and 117.30. The resistive filamentation[29] of electron beams is also observed in the simulations. Figures 117.31(a)–117.31(c) show the results of similar simulations in which the laser-spot diameter was increased to 20 μm. Figure 117.31 shows a similar trend as

TC8414JR
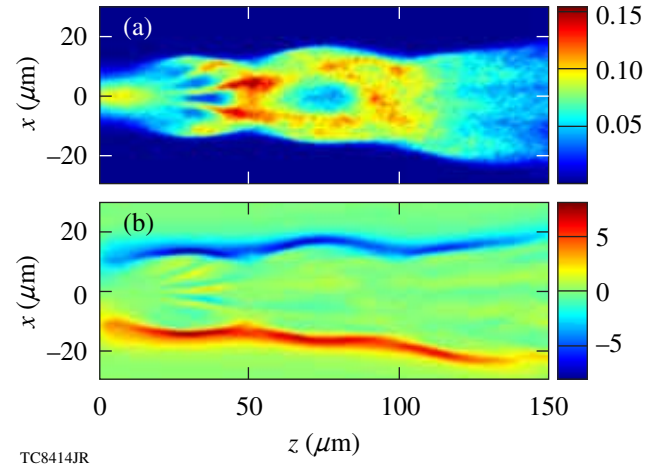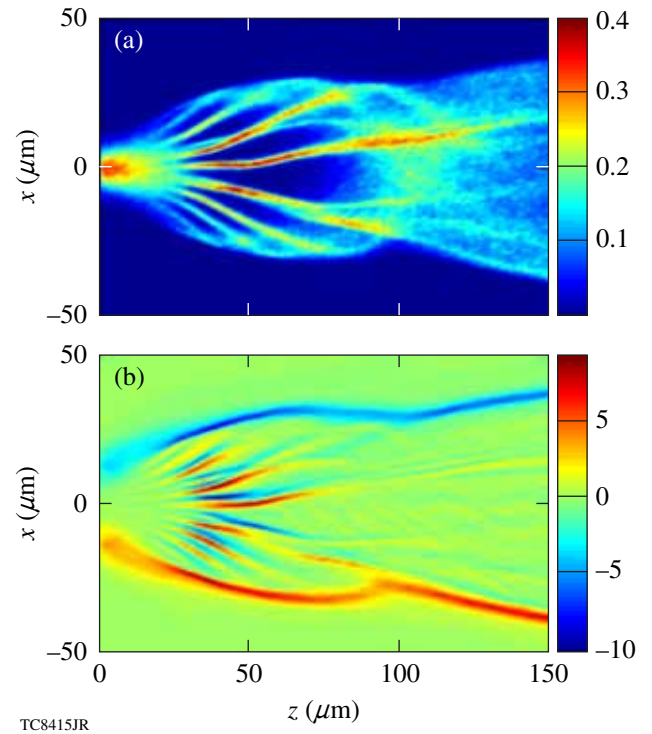
Figure 117.28

(a) Hot-electron density (in cm$^{-3} \times 10^{21}$) and (b) B_y component of magnetic field (in MG) 700 fs after the peak of the laser pulse in the simulation for a solid-density plastic target, and a laser pulse with a focal-spot diameter of 10 μm and a maximum intensity of 5×10^{18} W/cm^2.

TC8415JR

Figure 117.29

(a) Hot-electron density (in cm$^{-3} \times 10^{21}$) and (b) B_y component of magnetic field (in MG) 700 fs after the peak of the laser pulse in the simulation for a solid-density plastic target, and a laser pulse with a focal-spot diameter of 10 μm and a maximum intensity of 2×10^{19} W/cm^2.

Figs. 117.28–117.30—the electron collimation decreases when the laser intensity is increased. The same trend was observed in the solid-target electron-transport experiments. Electron collimation seems to be slightly weaker in the simulations with a larger spot size (Fig. 117.31), but the main dependence is on the laser intensity, in agreement with Ref. 10. Notice that more-sophisticated three-dimensional simulations are required for a better quantitative agreement of the electron-divergence half-angle in the experiments and simulations. The intensity dependence of the initial electron-divergence half-angle in the target, details of the resistivities for different target materials, and the ionization energy loss should also be accounted for. Such 3-D simulations are in progress.
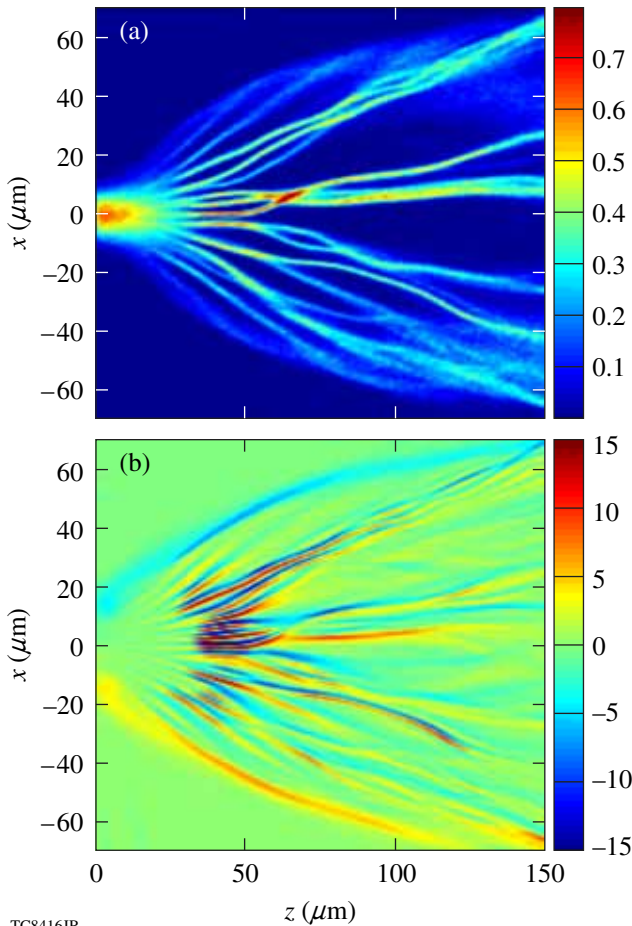
The first integrated fast-ignition experiments on OMEGA will be performed on imploding plastic targets, leading to plasmas with densities exceeding the solid-state value. The simulation of Fig. 117.32 uses a $C^{4+}H^{+}$ uniform plasma with a density of $10\times$ the solid density value ρ_{solid}, while in the simulation of Fig. 117.33, a Gaussian density distribution,

$$\rho = 100\,\rho_{solid} \times \exp\left(-\left\{[z(\mu m) - 90]^2 + x(\mu m)^2\right\}\Big/42^2\right),$$

is used to mimic the profile of a compressed fast-ignition target. In the simulation of Fig. 117.33 the density grows from ρ_{solid} at

TC8416JR

Figure 117.30

(a) Hot-electron density (in $cm^{-3} \times 10^{21}$) and (b) B_y component of magnetic field (in MG) 700 fs after the peak of the laser pulse in the simulation for a solid-density plastic target, and a laser pulse with a focal-spot diameter of 10 μm and a maximum intensity of 6×10^{19} W/cm^2
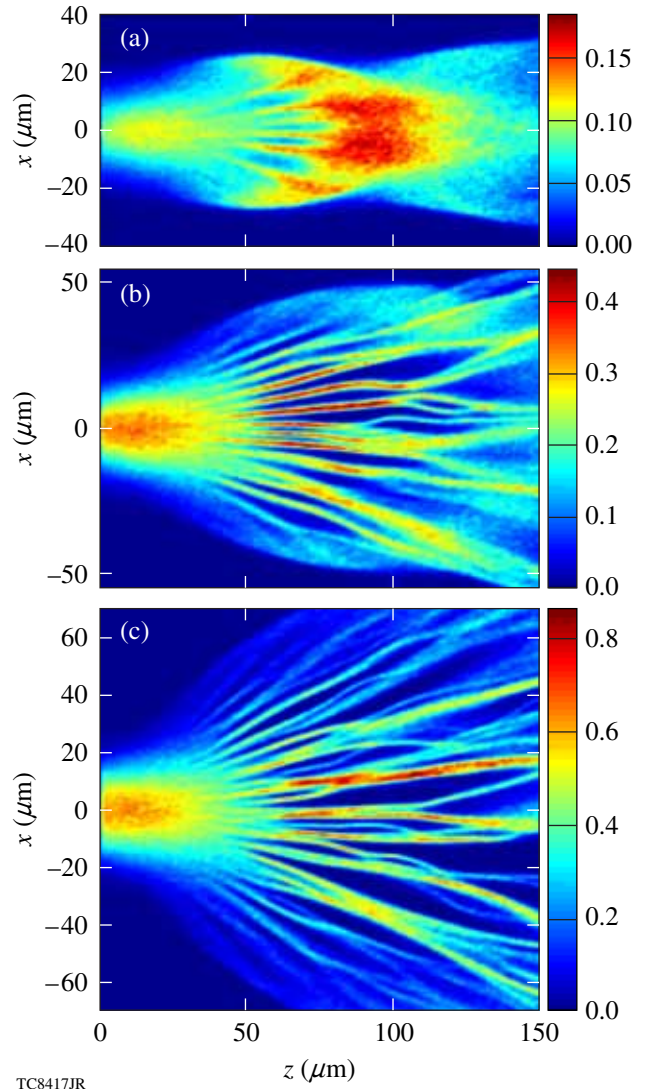

TC8417JR

Figure 117.31

Hot-electron density (in $cm^{-3} \times 10^{21}$) 700 fs after the peak of the laser pulse in the simulations for a solid-density plastic target, and a laser pulse with a focal-spot diameter of 20 μm and maximum intensities of (a) 5×10^{18} W/cm^2, (b) 2×10^{19} W/cm^2, and (c) 6×10^{19} W/cm^2.

the left-hand-side plasma boundary where the electron beam enters the plasma to $100 \times \rho_{\text{solid}}$ in the center of the target. The parameters of the laser pulse in both simulations are the same as in the simulation of Fig. 117.31(c): the spot diameter is 20 μm and the maximum intensity is 6×10^{19} W/cm^2.

In the simulation of Fig. 117.32 the hot-electron beam is well collimated over a length of 150 μm. The beam is also collimated in the simulation of Fig. 117.33, where it reaches the dense core and deposits its energy through collisions with plasma electrons and ions. The collimation is due to the generation of a large magnetic field on the electron-beam surface. These simulations show that magnetic collimation is effective at high laser intensities when the plasma is compressed above solid density as expected in fast-ignition targets.

Theoretical models of resistive collimation and filamentation were developed by Davies *et al.*[23] and Bell *et al.*[24] (collimation) and Gremillet *et al.*[29] (filamentation). The first estimate of the magnetic-field generation in fast-ignition plasmas was reported by Glinsky.[30] As the electron beam enters the plasma, it sets up an electrostatic and inductive ohmic electric field that opposes the hot-electron motion and drives a return current of background cold electrons,

$$\mathbf{E} = \eta \mathbf{j}_p \approx -\eta \mathbf{j}_h, \tag{1}$$

where $\mathbf{j}_p$ and $\mathbf{j}_h$ are the cold- and hot-electron current densities, respectively. Initially the two oppositely directed currents cancel each other and the magnetic field is absent. The resistive magnetic field grows in time according to Faraday's law,

$$\frac{\partial \mathbf{B}}{\partial t} = -c \nabla \times \mathbf{E}. \tag{2}$$

The net current density also grows according to Ampere's law $\mathbf{j} \approx (c/4\pi) \nabla \times \mathbf{B}$. The magnetic field of the beam pinches and collimates the hot electrons. A similar process occurs on local peaks of the current density leading to resistive filamentation. Since the plasma resistivity is a function of the electron temperature, the resistivity decreases as the plasma is heated by hot electrons. At sufficiently high temperatures, the electrical resistivity follows Spitzer's formula[25]

$$\eta = 10^{-2} Z f(Z) \ln \Lambda T_e^{-3/2} \ \Omega \times \text{cm}, \tag{3}$$

where Z is the ion charge state, $\ln \Lambda$ is the Coulomb logarithm, T_e is the electron temperature in eV, and $f(Z)$ changes from 0.52 to 0.3 when Z increases from 1 to infinity. The main heating mechanism for the background plasma is joule heating,
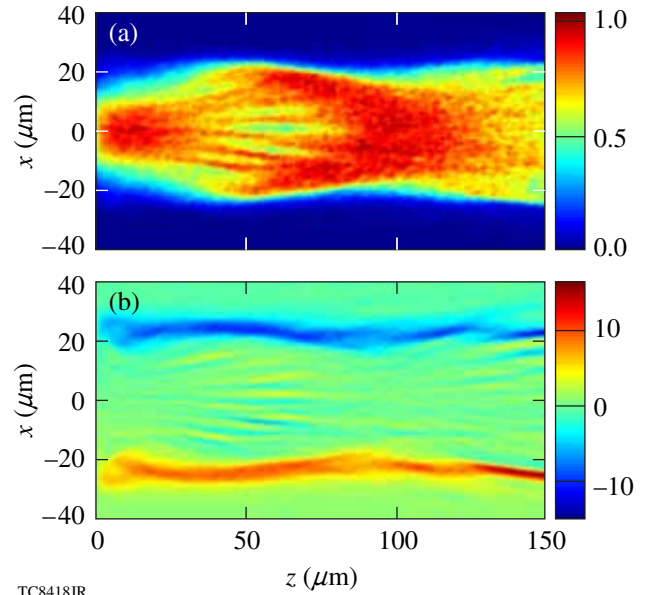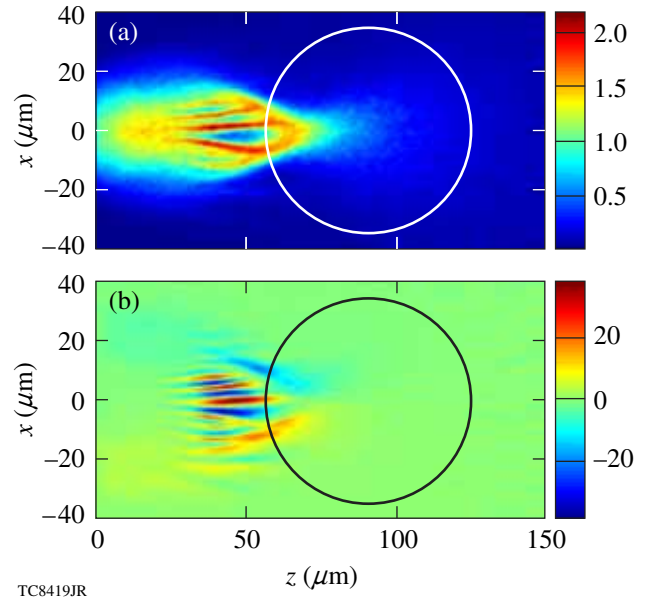

Figure 117.32
(a) Hot-electron density (in cm$^{-3} \times 10^{21}$) and (b) magnetic field (in MG) 700 fs after the peak of the laser pulse in the simulation for a compressed uniform plastic target and a laser pulse with a focal-spot diameter of 20 μm and a maximum intensity of 6×10^{19} W/cm^2.

Figure 117.33
(a) Hot-electron density (in cm$^{-3} \times 10^{21}$) and (b) magnetic field (in MG) 700 fs after the peak of the laser pulse in the simulation for a compressed plastic target with a Gaussian spatial density distribution, and a laser pulse with a focal-spot diameter of 20 μm and a maximum intensity of 6×10^{19} W/cm^2.

$$\frac{\partial T_e}{\partial t} = \frac{\eta j_p^2}{C}, \tag{4}$$

where $C = (3/2)n_e$ is the specific-heat capacity of an ideal electron gas and n_e is the electron density. Hot-electron collisions with cold plasma electrons become a dominant heating mechanism close to the dense core of the fast-ignition target (also suggested in Refs. 31 and 32). Plasma heating slows down the growth of the magnetic field and reduces the filamentation instability growth rate.

Magnetic collimation is not effective in the simulations of Figs. 117.29, 117.30, and 117.31(b)–117.31(c) because the plasma is heated too fast and the collimating magnetic field does not have enough time to grow before the resistivity decreases because of the high plasma temperature. On the other hand, in the simulations of Figs. 117.28 and 117.31(a), a strong magnetic field is generated as the plasma is heated slowly by the lower-intensity electron beam, thus keeping the resistivity low enough and allowing the field to grow. The mean energy of hot electrons in the simulations with a lower intensity is also smaller, according to the ponderomotive scaling[26]—a fact that facilitates the beam collimation. In the simulations of Figs. 117.32 and 117.33, the electron density is higher and the heating time is longer [see Eq. (4)]. Thus the collimating magnetic field has enough time to grow to a large enough strength to collimate high-energy electron beams. The resistive collimation of hot electrons can be induced more effectively if the laser pulse and the corresponding electron beam have a long rising front. In this case, a stronger collimating magnetic field can be generated during the rising pulse front, thus improving the collimation of the main beam.

In the next sections, the results of integrated *DRACO–LSP* simulations of cone-in-shell fast-ignition targets are presented. It is important to notice that many features of the electron-beam transport are similar to those obtained in the simplified simulations described in this section.

Integrated Simulations of Cone-in-Shell Plastic Targets for the Fast-Ignition Experiments at LLE

Integrated experiments on OMEGA using low-adiabat implosions of cone-in-shell plastic targets and petawatt heating pulses have begun at LLE. The targets are 40-μm-thick empty CD shells of ~870-μm outer diameter [Fig. 117.34(a)]. A hollow gold cone with an opening angle of 35° or 70° is inserted through a hole in the shell. The cone has a thickness of 10 μm inside the shell and ends in a 15-μm-thick flat tip, as shown in Fig. 117.34(b). The shell is compressed using a
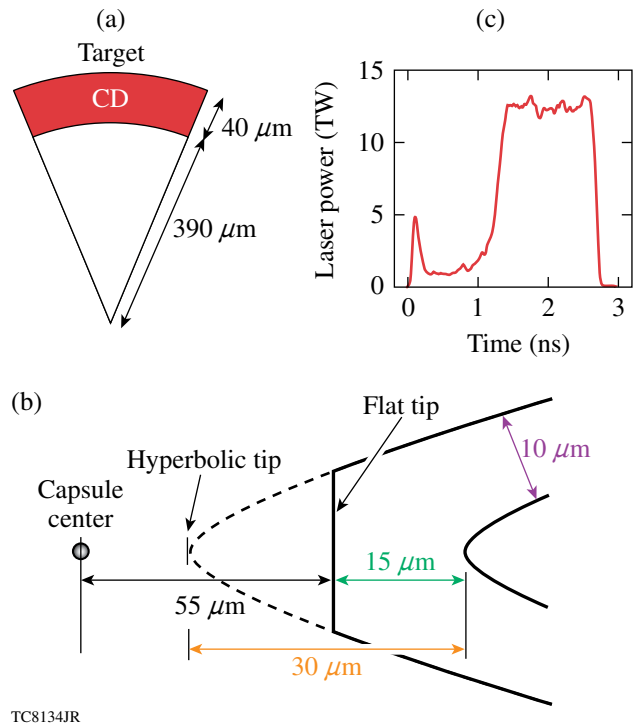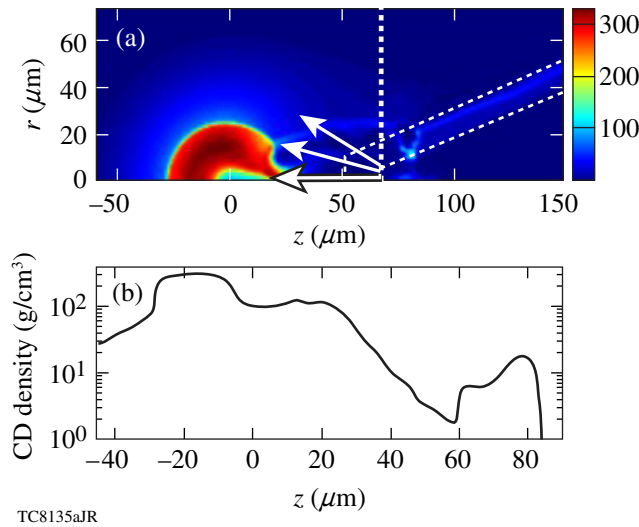

Figure 117.34
Fuel assembly in the integrated simulations for a cone-in-shell plastic target used in the fast-ignition experiments at LLE. Schematics of (a) a plastic shell and (b) a cone tip; (c) temporal profile of the laser pulse used for the target implosion.

351-nm-wavelength, highly shaped pulse of ~3-ns duration and ~20-kJ energy [Fig. 117.34(c)] designed to achieve high areal densities.[33] Previous implosion experiments using similar targets but without the OMEGA EP heating beam,[34] measured a neutron yield from D–D nuclear reactions of (2 to 3) × 10^7. The OMEGA EP petawatt laser delivers laser pulses with a 1.054-μm wavelength, energy up to 2.6 kJ, and a duration of about 10 ps.

We have carried out a set of integrated *DRACO–LSP* simulations of target heating for the OMEGA fast-ignition experiments. The simulations were performed for a 50° cone target. In the integrated simulations, *DRACO* was used to simulate the implosion of the plastic cone-in-shell target. *DRACO* and *LSP* were then integrated to simulate the target heating. Because of numerical difficulties related to the cone's gold opacities, the radiation transport was turned off in the *DRACO* simulations. Figure 117.35(a) shows the target density obtained in a *DRACO* simulation at $t = 3.54$ ns, close to the time of maximum areal density $\rho R \sim 0.8$ g/cm² (in the direction opposite to the cone). Figure 117.35(b) shows the density lineout through the z axis. The density in the compressed shell at this time was around 300 g/cm³. The initial position of the cone is shown by the white

Figure 117.35

(a) Target-density profile at the time of maximum ρR in the integrated simulations for the fast-ignition experiments at LLE. The dashed lines show the initial position of the cone. Hot electrons are injected in the simulations 70 μm from target center. (b) Lineout of CD density through the z axis. The density increase at $z > 60$ μm is due to compression by a shock reflected from the cone tip.

dashed lines. At $t = 3.54$ ns the cone tip was displaced away from the target center by a jet of high-pressure CD gas escaping through the hole in the compressed shell. Despite the fact that the plastic shell was initially empty, plastic was ablated from the inner shell surface and formed a hot, low-density plasma inside the shell. The cone tip not only shifted at this time but was also crushed, and a plastic/gold plasma filled the interior of the cone. We are currently working on optimizing the cone-in-shell implosions,[8] by varying the cone-tip thickness and distance from the target center, to preserve the integrity of the cone tip at the time of maximum ρR. Here we focus solely on the hot-electron transport in the plastic plasma outside the cone tip. We assume that it is possible to optimize the cone-in-shell implosion and that the hot electrons penetrating through the cone tip reach the plastic plasma. These assumptions will be verified in future integrated simulations.

In the present simulations hot electrons were injected at the time of maximum ρR in the plastic plasma located past the cone tip, 70 μm away from the target center. The plastic plasma was assumed to be fully ionized in the simulations described in this section. The hot-electron beam had a square profile in time with a duration of 10 ps and a Gaussian radial profile with FWHM of 20 μm. We assume that the beam was generated by an OMEGA EP laser pulse with a similar profile, an energy of 2.6 kJ, on-axis intensity of 5.4×10^{19} W/cm^2, and energy conversion efficiency to hot electrons of 30%. For a given

energy, the pulse intensity in the experiment can be varied by changing the pulse duration. According to the ponderomotive scaling,[26] the mean energy of hot electrons also changes. In the simulations hot electrons were generated with a relativistic Maxwellian energy-distribution function, and the mean energy was varied from 1.2 to 2.4 MeV to account for the intensity changes. The angular spread of hot electrons from the cone tip was estimated based on previous experimental results. Hot-electron divergence of about 20° (half-angle) has been reported in earlier cone-target experiments.[2,35] Hot-electron divergence could increase with an increasing thickness of the cone tip because of a strong electron scattering in the gold. The initial divergence was taken as a free parameter in the simulations and varied from 20° to 60° (HWHM, half-angle).

Figure 117.36 shows snapshots of the (a) plasma density, (b) electron-beam density, and (c) azimuthal magnetic field 6 ps after the beginning of the hot-electron beam in the simulation with a mean electron energy of 2 MeV and angular divergence of 20° (half-angle). Figure 117.36(d) shows the temperature of the plasma before the electron beam arrives and Fig. 117.36(e) shows the plasma temperature increase caused by the heating by hot electrons. Figure 117.36(b) shows that the electron beam is well collimated by the self-generated resistive magnetic field. Interestingly, the hot electrons at the axis are somewhat deflected in the $+r$ direction when they approach the core. This is due to the magnetic field (having a negative sign) generated in the hot gas escaping from the center of the target through the hole in the compressed shell. Indeed, the Spitzer plasma resistivity [Eq. (3)] is a decreasing function of temperature. According to Eqs. (1) and (2), in the region of a nonuniform resistivity, a magnetic field of such a sign is generated, deflecting the hot electrons to the region of a higher resistivity. The hot electrons are deflected from the low-density hot-gas region to the dense core, increasing the coupling of hot electrons with the core in the experiment.

Figure 117.36(e) shows that the maximum temperature increase due to hot electrons is about 2.5 keV. It is achieved, however, in the low-density part of the plasma [see the plasma density contours in Fig. 117.36(e)]. The maximum temperature increase in the dense core is about 1 keV in the right-hand side of the core.

Figure 117.37 shows the (a) electron-beam density and (b) azimuthal magnetic field 6 ps after the beginning of the hot-electron beam propagation. In this simulation the electron-beam divergence was increased to 60° (half-angle). The plasma temperature increase due to hot electrons is shown in

Fig. 117.37(c). Even for such a large angular divergence, a large fraction of hot electrons were still collimated by the resistive magnetic field and reached the dense core. (See also Fig. 117.39 showing the hot-electron-density lineouts near the dense core in the simulations of Figs. 117.36–117.38.) Some electrons, however, escape in the radial direction. The temperature increase in the dense core is about 500 eV maximum.
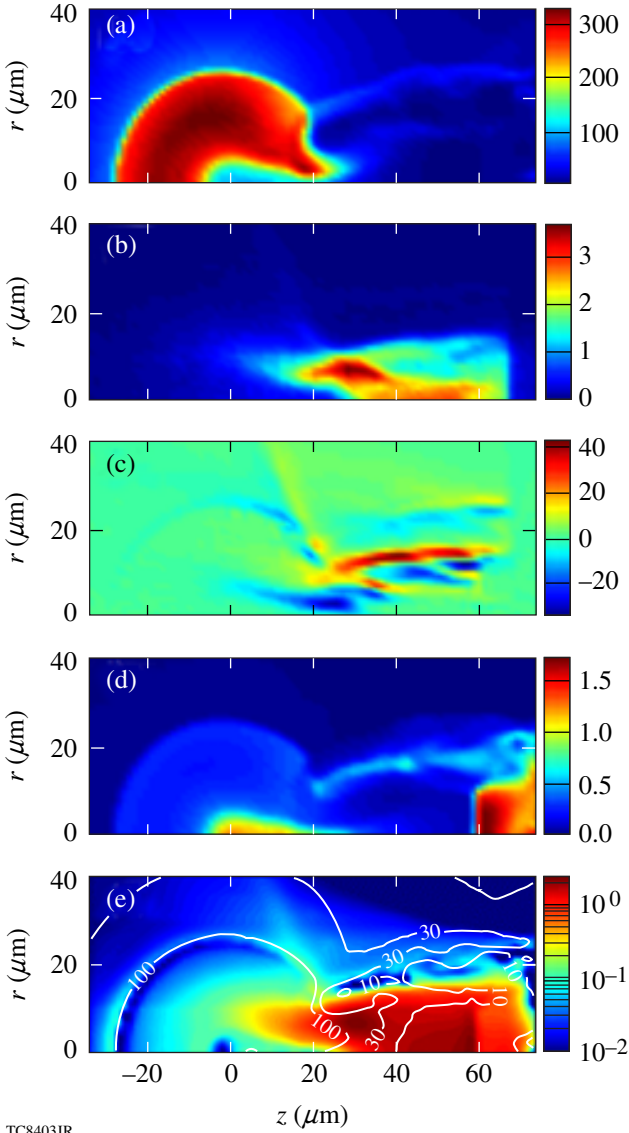

TC8403JR

Figure 117.36

(a) Plasma density (in g/cm^3), (b) hot-electron density (in cm^{-3} × 10^{21}), and (c) azimuthal magnetic field (in MG) 6 ps after the beginning of the hot-electron beam with an initial divergence of 20° (half-angle). (d) Plasma temperature (in keV) before the electron-beam injection. (e) Ion-temperature increase (in keV) in the end of the hot-electron pulse; plasma density in g/cm^3 contours (white curves) are also shown.
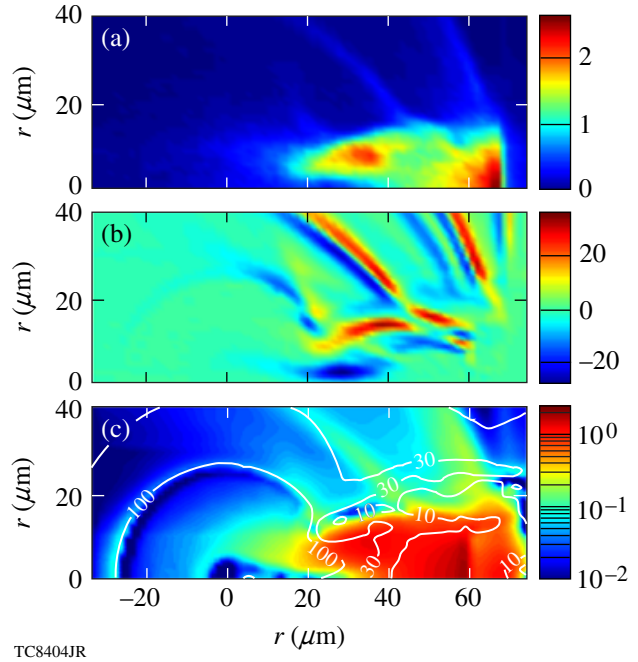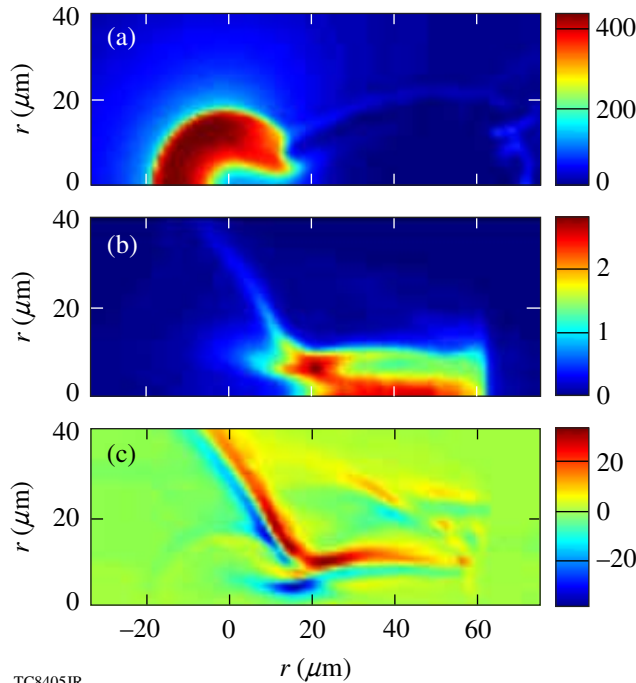

TC8404JR

Figure 117.37

(a) Hot-electron density (in cm^{-3} × 10^{21}) and (b) azimuthal magnetic field (in MG) 6 ps after the beginning of the hot-electron beam with an initial divergence of 60° (half-angle). (c) Ion-temperature increase (in keV) in the end of the hot-electron pulse; plasma density in g/cm^3 contours (white curves) are also shown.

Figure 117.38 shows the results of a simulation in which the electron-beam parameters were kept the same as in the simulation of Fig. 117.36, but the electron beam was injected 60 ps earlier. At this time the core radius is smaller and the maximum density is higher [compare Figs. 117.36(a) and 117.38(a)] because the maximum ρR is reached when the target begins to expand. Figures 117.38(b) and 117.38(c) show that the electron beam was highly deflected by the magnetic field in the escaping hot gas, and many electrons missed the dense core. This happened because a strong defocusing magnetic field was generated and shifted in the +r direction due to a larger opening in the shell at this time. The dense core outer radius was also smaller, so more hot electrons missed the core. If not for this effect, earlier injection of hot electrons could be beneficial since the cone tip's integrity can be preserved before it is crushed by the hot-gas jet from the compressed shell.

Figure 117.40 summarizes the results of our simulations by plotting the fraction of hot-electron-beam energy deposited in the dense core (in the region with density ρ > 80 g/cm^3) as a function of the mean electron energy and angular divergence. This fraction is a weak function of the mean electron energy and decreases from about 50% to 25% when the angular divergence is increased from 20° to 60° (half-angle).

The calculated neutron yield from D−D nuclear reactions was maximum for lower angular divergences. The yield increase caused by the hot-electron-beam heating was about 3×10^9 neutrons for a divergence of 20° (half-angle).

TC8405JR

Figure 117.38
(a) Plasma density (in g/cm^3), (b) hot-electron density (in cm$^{-3} \times 10^{21}$), and (c) azimuthal magnetic field (in MG) 6 ps after the beginning of the hot-electron beam with an initial divergence of 20° (half-angle), injected 60 ps earlier than in the simulation in Fig. 117.36.
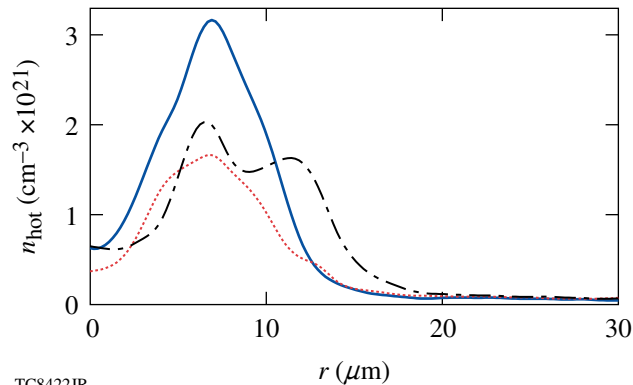
TC8422JR

Figure 117.39
Radial lineouts of the hot-electron density near the dense core: at $z = 25$ μm in Figs. 117.36(b) (solid line) and 117.37(a) (dotted line), and at $z = 13$ μm in Fig. 117.38(b) (dashed−dotted line).
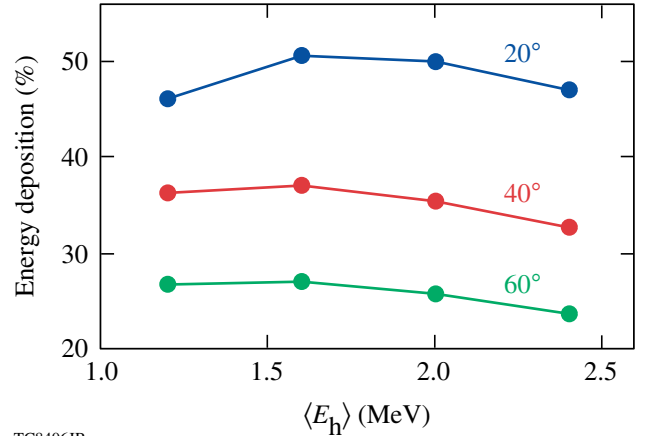
TC8406JR

Figure 117.40
Fraction of the electron-beam energy deposited in the dense core (in the region with density $\rho > 80$ g/cm^3).

It is important to mention that more work is necessary to optimize cone-in-shell implosions to preserve the integrity of the cone tip. The transport of hot electrons through the cone tip also must be addressed through dedicated hybrid-PIC simulations. For this purpose *LSP* must be modified to model the ionization of the high-*Z* cone material, using the quantum equations of state.[36] We expect that the angular divergence of the hot electrons will increase due to the enhanced electron scattering in the gold. Tens- to hundreds-of-megagauss resistive magnetic fields are expected in the cone because of the high collisionality of the return current. In such fields, the Alfvén limit can be reached for the filaments or for the entire beam. Magnetic fields can develop at plasma discontinuities (inner cone surface or cone−plasma interface) and cause a surface transport and/or trapping of hot electrons. Finally, an inevitable laser prepulse can create extended regions of pre-plasma inside the cone, increasing the thickness of the high-*Z* cone material through which the hot electrons propagate.

Conclusion
This article has described the latest results from a set of integrated simulations of the implosion, hot-electron transport, and ignition of direct-drive, fast-ignition cone-in-shell plastic targets, using the hydrodynamic code *DRACO* and the hybrid-PIC code *LSP*. *LSP* simulations of electron transport in solid-density plastic targets have also been presented. These simulations show the importance of self-generated resistive magnetic fields to the transport of hot electrons. *LSP* simulations of solid-density plastic targets show that the effectiveness of magnetic collimation of laser-generated hot electrons decreases with an increase in the laser intensity, in agreement

with solid-target electron-transport experiments. It has also been shown that hot-electron collimation for high-intensity petawatt laser pulses is possible in compressed plastic targets with densities relevant to integrated fast-ignition experiments on OMEGA.

Performance of the cone-in-shell plastic targets developed for integrated fast-ignition experiments at LLE has been investigated using integrated simulations of implosion, hot-electron transport, and target heating. In the present simulations, only the hot-electron transport through the plastic plasma has been investigated. The hot-electron transport through the cone was not simulated. Resistive collimation of hot electrons was found to effectively reduce the hot-electron angular spread and increase the coupling efficiency of hot electrons to the core. Resistive collimation is effective even for electron beams with a large angular spread, up to 60° (half-angle). The coupling efficiency of hot electrons with the target core is about 50% for initial electron divergence of 20° (half-angle), decreasing to 25% for initial divergence of 60°. The integrated simulations predict a neutron-yield enhancement from D−D nuclear reactions of about 10^9 neutrons, which can be easily measured in the experiments. This is significantly more than the implosion neutron yield measured for such targets without a petawatt laser beam.

ACKNOWLEDGMENT

REFERENCES

1. M. Tabak *et al.*, Phys. Plasmas **1**, 1626 (1994).

2. R. Kodama *et al.*, Nature **412**, 798 (2001); R. Kodama *et al.*, Nature **418**, 933 (2002).

3. K. A. Tanaka *et al.*, Phys. Plasmas **10**, 1925 (2003); P. A. Norreys, K. L. Lancaster, C. D. Murphy, H. Habara, S. Karsch, R. J. Clarke, J. Collier, R. Heathcote, C. Hernandez-Gomez, S. Hawkes, D. Neely, M. H. R. Hutchinson, R. G. Evans, M. Borchesi, L. Romagnani, M. Zepf, K. Akli, J. A. King, B. Zhang, R. R. Freeman, A. J. MacKinnion, S. P. Hatchett, P. Patel, R. Snavely, M. H. Key, A. Nikroo, R. Stephens, C. Stoeckl, K. A. Tanaka, T. Norimatsu, Y. Toyama, and R. Kodama, Phys. Plasmas **11**, 2746 (2004).

4. R. Betti and C. Zhou, Phys. Plasmas **12**, 110702 (2005).

5. A. A. Solodov, R. Betti, J. A. Delettrez, and C. D. Zhou, Phys. Plasmas **14**, 062701 (2007).

6. A. A. Solodov, K. S. Anderson, R. Betti, V. Gotcheva, J. Myatt, J. A. Delettrez, S. Skupsky, W. Theobald, and C. Stoeckl, Phys. Plasmas **15**, 112702 (2008).

7. P. B. Radha, T. J. B. Collins, J. A. Delettrez, Y. Elbaz, R. Epstein, V. Yu. Glebov, V. N. Goncharov, R. L. Keck, J. P. Knauer, J. A. Marozas, F. J. Marshall, R. L. McCrory, P. W. McKenty, D. D. Meyerhofer, S. P. Regan, T. C. Sangster, W. Seka, D. Shvarts, S. Skupsky, Y. Srebro, and C. Stoeckl, Phys. Plasmas **12**, 056307 (2005).

8. K. S. Anderson, A. A. Solodov, R. Betti, and P. W. McKenty, Bull. Am. Phys. Soc. **53**, 53 (2008).

9. D. R. Welch *et al.*, Phys. Plasmas **13**, 063105 (2006).

10. J. S. Green, V. M. Ovchinnikov, R. G. Evans, K. U. Akli, H. Azechi, F. N. Beg, C. Bellei, R. R. Freeman, H. Habara, R. Heathcote, M. H. Key, J. A. King, K. L. Lancaster, N. C. Lopes, T. Ma, A. J. MacKinnon, K. Markey, A. McPhee, Z. Najmudin, P. Nilson, R. Onofrei, R. Stephens, K. Takeda, K. A. Tanaka, W. Theobald, T. Tanimoto, J. Waugh, L. Van Woerkom, N. C. Woolsey, M. Zepf, J. R. Davies, and P. A. Norreys, Phys. Rev. Lett. **100**, 015003 (2008).

11. J. C. Adam, A. Héron, and G. Laval, Phys. Rev. Lett. **97**, 205006 (2006).

12. S. Atzeni, Phys. Plasmas **6**, 3316 (1999).

13. S. Atzeni, A. Schiavi, and C. Bellei, Phys. Plasmas **14**, 052702 (2007).

14. A. A. Solodov and R. Betti, Phys. Plasmas **15**, 042707 (2008).

15. C. K. Li and R. D. Petrasso, Phys. Rev. E **70**, 067401 (2004); C. K. Li and R. D. Petrasso, Phys. Rev. E **73**, 016402 (2006).

16. E. M. Lifshitz and L. P. Pitaevskiĭ, *Physical Kinetics*, 1st ed., Course of Theoretical Physics, Vol. 10 (Pergamon Press, Oxford, 1981), Chap. 4.

17. R. R. Freeman *et al.*, Fusion Sci. Technol. **49**, 297 (2006); M. H. Key, Phys. Plasmas **14**, 055502 (2007).

18. Y. T. Lee and R. M. More, Phys. Fluids **27**, 1273 (1984).

19. J. J. Honrubia and J. Meyer-ter-Vehn, J. Phys., Conf. Ser. **112**, 022055 (2008); S. Atzeni *et al.*, Phys. Plasmas **15**, 056311 (2008).

20. M. Tatarakis *et al.*, Phys. Rev. Lett. **81**, 999 (1998).

21. M. Borghesi *et al.*, Phys. Rev. Lett. **83**, 4309 (1999).

22. L. Gremillet *et al.*, Phys. Rev. Lett. **83**, 5015 (1999).

23. J. R. Davies *et al.*, Phys. Rev. E **56**, 7193 (1997).

24. A. R. Bell and R. J. Kingham, Phys. Rev. Lett. **91**, 035003 (2003).

25. L. Spitzer Jr. and R. Härm, Phys. Rev. **89**, 977 (1953); L. Spitzer, *Physics of Fully Ionized Gases*, 2nd rev. ed., Interscience Tracts on Physics and Astronomy (Interscience, New York, 1962).

26. S. C. Wilks and W. L. Kruer, IEEE J. Quantum Electron. **33**, 1954 (1997).

27. F. N. Beg *et al.*, Phys. Plasmas **4**, 447 (1997).

28. R. P. J. Town *et al.*, Nucl. Instrum. Methods Phys. Res. A **544**, 61 (2005).

29. L. Gremillet, G. Bonnaud, and F. Amiranoff, Phys. Plasmas **9**, 941 (2002).

30. M. E. Glinsky, Phys. Plasmas **2**, 2796 (1995).

31. B. Chrisman, Y. Sentoku, and A. J. Kemp, Phys. Plasmas **15**, 056309 (2008).

32. J. J. Honrubia and J. Meyer-ter-Vehn, Nucl. Fusion **46**, L25 (2006).

33. C. D. Zhou, W. Theobald, R. Betti, P. B. Radha, V. A. Smalyuk, D. Shvarts, V. Yu. Glebov, C. Stoeckl, K. S. Anderson, D. D. Meyerhofer, T. C. Sangster, C. K. Li, R. D. Petrasso, J. A. Frenje, and F. H. Séguin, Phys. Rev. Lett. **98**, 025004 (2007).

34. C. Stoeckl, T. R. Boehly, J. A. Delettrez, S. P. Hatchett, J. A. Frenje, V. Yu. Glebov, C. K. Li, J. E. Miller, R. D. Petrasso, F. H. Séguin, V. A. Smalyuk, R. B. Stephens, W. Theobald, B. Yaakobi, and T. C. Sangster, Phys. Plasmas **14**, 112702 (2007).

35. R. B. Stephens *et al.*, Phys. Rev. Lett. **91**, 185001 (2003).

36. R. M. More *et al.*, Phys. Fluids **31**, 3059 (1988).